

This work has been submitted to the IEEE for possible publication. Copyright may be transferred without notice, after which this version may no longer be accessible.

Digital Object Identifier

A Parameterized Nonlinear Magnetic Equivalent Circuit for Design and Fast Analysis of Radial Flux Magnetic Gears

DANIAL KAZEMIKIA, and MATTHEW C. GARDNER, (Member, IEEE)

Department of Electrical Engineering, University of Texas at Dallas, Richardson, TX 75080 USA

Corresponding author: D. Kazemikia (email: danial.kazemikia@utdallas.edu).

arXiv:2406.08375v2 [eess.SY] 28 Sep 2024

ABSTRACT Magnetic gears offer advantages over mechanical gears, including contactless power transfer, but require robust analysis tools for optimization and commercialization. This study proposes a fast and accurate 2D nonlinear magnetic equivalent circuit (MEC) model for radial flux magnetic gears (RFMG) with bridges. The model, featuring a parameterized gear geometry and adjustable flux tube distribution, accommodates nonlinear effects like magnetic saturation while maintaining quick simulation times. Comparison with a nonlinear finite element analysis (FEA) model demonstrates the MEC's accuracy in torque and flux density predictions across diverse designs. The high accuracy of this model is then confirmed by a parametric optimization study of 140,000 designs, achieving close agreement with FEA torque predictions, with simulations running up to 100 times faster.

INDEX TERMS Design optimization, finite element analysis, magnetic equivalent circuit, magnetic gear, magnetic saturation, mesh-flux analysis, Newton-Raphson, nonlinear permeability, permeance network, radial flux, reluctance network

I. INTRODUCTION

MAGNETIC gears (MGs) are a power transmission technology that leverages magnetic fields to convert mechanical energy between high-speed, low-torque rotation and low-speed, high-torque rotation. Unlike conventional mechanical gear systems, MGs operate without physical contact, providing inherent overload protection and reducing maintenance challenges. This contactless operation enables effective isolation between input and output shafts, potentially resulting in more reliable performance and less noise [1]. With proposed applications ranging from wind [2]–[4] and wave energy harvesting [5] to traction applications [6], [7], such as electric vehicles [8]–[10], and aircraft propulsion [11]–[13], MGs offer promising solutions for robust and efficient energy transmission. NASA's exploration of magnetic gearing for electric aviation propulsion underscores its technological potential [14]–[17].

As the most common topology, radial flux MGs (RFMGs) have demonstrated the greatest experimental torque densities reported thus far [18]–[20]. As depicted in Fig. 1, this topology, consists of three concentric rotors: two permanent magnet (PM) rotors and the magnetically permeable modula-

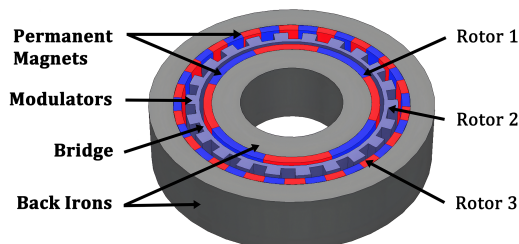


FIGURE 1. Coaxial radial flux magnetic gear with surface-mounted PMs.

tors between them. The modulator count (Q_2) relates to the number of inner and outer PM pole pairs, (P_1) and (P_3), by:

$$Q_2 = P_1 + P_3 \quad (1)$$

The maximum gear ratio (G) is achieved by fixing Rotor 3, resulting in

$$G|_{\omega_3=0} = \frac{\omega_1}{\omega_2} = \frac{Q_2}{P_1} \quad (2)$$

where ω_1 , ω_2 , and ω_3 are the speeds of Rotors 1, 2, and 3, respectively.

A critical feature of these modulators is a bridge that connects them, providing structural support and simplify-

ing manufacturing by stabilizing the modulators against the strong magnetic forces generated between the two sets of PMs. However, the bridge also creates a flux leakage path, reducing the slip torque [3], [21], [22]. A relatively thin bridge can mitigate PM eddy current losses, slightly improving efficiency compared to designs without a bridge or with a thicker bridge [21], [23]. Nonetheless, the bridge may experience significant magnetic saturation, requiring a nonlinear model for accurate analysis.

Despite advancements, RFMGs face challenges in competing with mechanical counterparts in terms of size, weight, and cost [24]. To fully achieve the potential of MGs, accurate and effective analysis tools are required. Finite element analysis (FEA) is the most often used tool due to its accuracy, accessibility, and robustness in capturing complex nonlinear effects. However, FEA has high computational costs, especially in intricate designs, which can increase the simulation run times [25]. In contrast, analytical models and winding function theory (WFT) offer faster computations but may lack design flexibility and accuracy, particularly in representing complex flux paths and nonlinearities [26], [27]. However, high-resolution magnetic equivalent circuit (MEC) models, which are sometimes referred to as reluctance networks, strike a balance between accuracy and computational efficiency, making them suitable for optimization studies [25], [28].

Previously, [28], [29] introduced a parameterized high-resolution MEC for simplistic RFMGs that accurately tracked design trends. However, it did not account for nonlinearity and became less accurate when ferromagnetic components became thin and saturated [29]. While, some previous papers have proposed nonlinear MECs for MGs [30]–[32], these papers did not establish systematic rules for the discretization of the geometry or for assessing convergence of the iterative nonlinear solver. Thus, their models were not demonstrated to yield consistent accuracy across a wide range of designs. Additionally, previous works did not evaluate designs with bridges between the modulators, which are commonly used to simplify manufacturing and increase the rigidity of the modulators [1], [3], [4], [7], [10], [20]–[23], [33]–[35]. These bridge-less designs experience much less saturation than similar designs with bridges, and, as demonstrated in [29], the nonlinearity in the design often has minimal impacts on the flux density distributions and torques. On the other hand, it is critical to account for nonlinearity when evaluating RFMGs with bridges between modulators. As an example, Fig. 2 illustrates a 2D design with bridges experiencing saturation. For this design, linear and nonlinear FEA predict slip torques of 1.2 kNm and 6.7 kNm, respectively, which is an 82% discrepancy. The significant disparity between the two results underscores the importance of modeling the nonlinearity. Therefore, this paper presents a highly parameterized nonlinear MEC model and evaluates its effectiveness across a wide range of MG designs with bridges.

II. IMPLEMENTATION

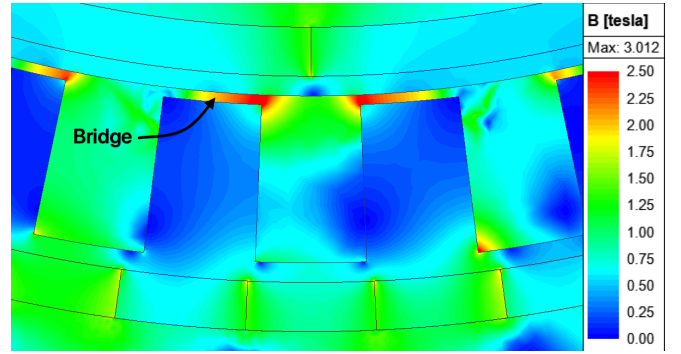


FIGURE 2. Flux density (B) based on nonlinear FEA in a sample RFMG with bridges

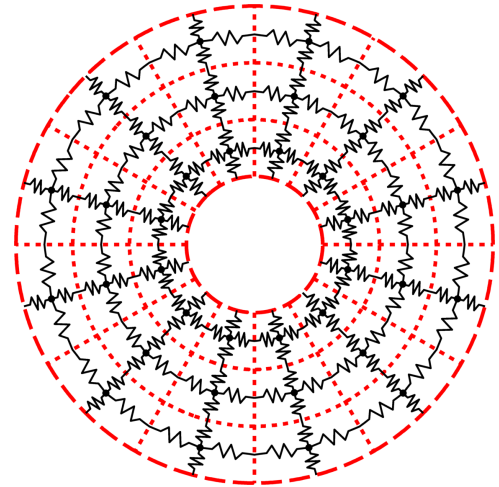


FIGURE 3. Radial and angular layers and mesh node cells in a simple MEC example

A. MESHING AND THE NODE CELL

By discretizing (meshing) the MG into radial and angular (tangential) layers, the systematic, parameterized 2D MEC implemented in [28] and [29] is utilized. Fig. 3 shows an example of a source-free MEC, which consists of 3 radial layers, and 12 tangential layers. The boundaries of these layers are denoted by the dotted lines. The overlap of each radial layer with each angular layer defines an arc-shaped region called a 2D node cell. As depicted in Fig. 3 each 2D node cell has four reluctances, two oriented radially and two oriented tangentially. These reluctances represent flux tubes that connect each boundary of the node cell to the center of the node cell, allowing positive or negative flux to flow from the center of the node cell to each of its boundaries.

If a flux tube contains a PM magnetized in the direction of the flux tube, an MMF source is placed in series with the reluctance. (In this paper, MMF sources only appear in the flux tubes oriented radially within the PMs since only radially magnetized PMs are considered.) These flux tubes are represented using the equivalent circuit configuration depicted in Fig. 4, in which \mathcal{R}_{rad} denotes the reluctance of the radial flux tube with the permeability of μ_{PM} , \mathcal{F}_{inj} signifies

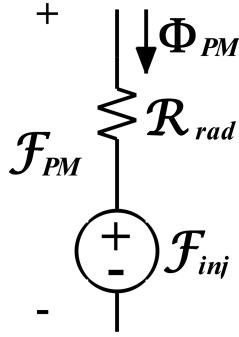


FIGURE 4. Equivalent circuit representation of a radially oriented permanent magnet flux tube

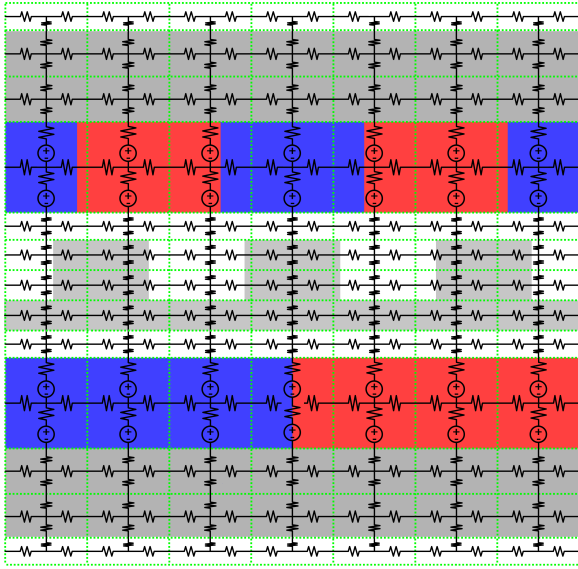


FIGURE 5. MEC overlaid on an example unrolled RFMG

the equivalent magnetomotive force (MMF) injected by the PM, \mathcal{F}_{PM} represents the MMF drop across the flux tube, and Φ_{PM} indicates the magnetic flux in the flux tube.

In this study, as in [28], the MEC mesh is distributed throughout the geometry as illustrated in Fig. 5, depicting a very coarse mesh overlaid on the unrolled representation of an RFMG with $P_1 = 1$, $P_3 = 2$, and $Q_2 = 3$. This mesh distribution divides the geometry into an equal number of angular layers. It partitions the RFMG into eight distinct radial regions, the inner back iron, inner PMs, inner air gap, bridge, modulators, outer air gap, outer PMs, and the outer back iron. The meshing also extends to the air inside the inner back iron and outside the outer back iron. Each of these ten radial regions consists of several radial layers. The user determines the number of radial layers in each region and the number of angular layers based on the tradeoff between analysis speed and accuracy.

B. THE SYSTEM OF NONLINEAR EQUATIONS

The MEC model is developed based on mesh-flux analysis, derived from Ampere's circuital law, where the circulating

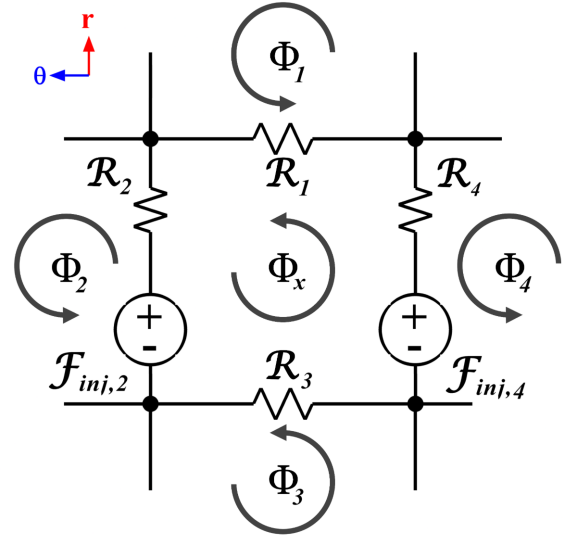


FIGURE 6. 2D mesh loop schematic

magnetic fluxes in each mesh loop represent an independent unknown variable. Mesh-flux analysis is utilized like Kirchhoff's voltage law is employed in the mesh-current analysis of electrical circuits. As an example, Fig. 6 depicts a mesh loop of the MEC, featuring node cells in the PMs. Loops outside the PMs are modeled similarly, except they lack the MMF sources. Applying Ampere's law to the mesh loop in Fig. 6, results in a mesh-flux equation of the form

$$\sum_{i=1}^4 \mathcal{R}_i(\Phi)(\Phi_x - \Phi_i) = f_{inj,4} - f_{inj,2} \quad (3)$$

where the left-hand term represents the sum of the reluctances within the mesh multiplied by their respective fluxes. This term characterizes the MMF drop attributed to the reluctances in the loop and equals the sum of the injected MMF sources in that loop. In mesh-flux analysis, reluctances are utilized instead of permeances for ease of calculation. The reluctance of each flux tube is computed similarly to [28], except that, to represent saturation in ferromagnetic materials, the permeability depends on the flux density within the node cell.

The system of nonlinear equations describing the 2D MEC model is achieved by representing every mesh loop in the MEC by a mesh flux equation of the same basic form shown in (3). If the MEC consists of N_{AL} number of angular layers and N_{RL} number of radial layers, the number of mesh loops N equals $N_{AL} \times (N_{RL} - 1)$. This MEC model can be expressed in the matrix form as

$$[\mathcal{R}(\Phi)]_{N \times N} [\Phi]_{N \times 1} = [f]_{N \times 1} \quad (4)$$

where \mathcal{R} is the reluctance matrix, Φ is the column vector of unknown mesh fluxes, and f is the column vector of the algebraic sum of the MMFs injected by PMs in each loop.

In the reluctance matrix, \mathcal{R} , the i^{th} row corresponds to the i^{th} mesh loop in the MEC and contains the reluctance

coefficients for that loop's flux equation, such as those shown on the left side of (3). The j^{th} column in \mathcal{R} corresponds to the j^{th} loop flux in the MEC. Entry $\mathcal{R}_{(i,j)}$ in \mathcal{R} contains the reluctance coefficient which describes the impact of the j^{th} loop's flux on the net MMF drop around the i^{th} loop. Each diagonal entry $\mathcal{R}_{(i,i)}$ in \mathcal{R} contains the positive sum of all reluctances surrounding the i^{th} loop. The reluctance coefficient of Φ_x in (3) illustrates a diagonal entry within the matrix representation of the system of equations, indicating the impact of the corresponding loop's flux on the net MMF drop around the loop. Each off-diagonal entry $\mathcal{R}_{(i,j)}$ (where $i \neq j$) in \mathcal{R} contains the negative value of the reluctance through which both the i^{th} and j^{th} loop fluxes pass. If those loops are not adjacent, the corresponding entry in \mathcal{R} is zero. The reluctance coefficients $\mathcal{R}_1, \mathcal{R}_2, \mathcal{R}_3,$ and \mathcal{R}_4 in (3) exemplify off-diagonal entries in the matrix form of the system of equations. Since all the reluctances in the MEC are bidirectional, the matrix \mathcal{R} is always symmetric. Also, each loop in the MEC has four adjacent loops, except for the innermost and outermost loops, which lack adjacent loops on their radial inside and outside, respectively. As a result, all the rows in \mathcal{R} have five non-zero entries: one for each adjacent loop, as well as the diagonal entry in that row, except for the rows corresponding to the innermost and outermost loops, which have four non-zero entries. If the model exhibits symmetry, the analysis can be simplified by solving only the subset of equations corresponding to the mesh loops within a symmetrical fraction of the model.

Mesh-flux analysis was chosen over the node-MMF analysis used in [28], [29] due to a convergence issue encountered when solving the system of nonlinear equations with the Newton-Raphson method. Mesh-flux analysis directly outputs flux, from which flux density can easily be calculated to update permeability. On the other hand, node-MMF analysis calculates MMF; then, the reluctances, which depend on flux density, must be used to determine magnetic flux. However, this requires the use of reluctances from the previous iteration and can prevent convergence in many cases.

C. NONLINEAR ANALYSIS WITH NEWTON-RAPHSON METHOD

The 2D MEC model is analyzed by solving the following system of nonlinear equations, which can be rewritten from (4) as

$$\mathcal{R}(\Phi) \times \Phi - f = 0 \quad (5)$$

This nonlinear equation is solved iteratively using the Newton-Raphson method, as it generally offers relatively fast convergence [36]. Substituting the calculated Φ for the k^{th} iteration back into the left-hand side of (5) and updating the reluctances in \mathcal{R} yields the residual matrix, $r(\Phi)$, as in

$$\mathcal{R}(\Phi_k) \times \Phi_k - f = r(\Phi_k) \quad (6)$$

where the goal of the Newton-Raphson method is to find Φ_k such that the residual becomes a column vector of zeros.

To apply the Newton-Raphson method to (6), the following equation is iteratively used to solve for Φ , the root of the equation:

$$\Phi_{k+1} = \Phi_k - \frac{r(\Phi_k)}{r'(\Phi_k)} \quad (7)$$

Here, $r'(\Phi)$ is the Jacobian of $r(\Phi)$, which contains the partial derivatives of this multivariate function with respect to the mesh fluxes. The Jacobian matrix elements are calculated similarly to the reluctance matrix, $\mathcal{R}(\Phi)$, but using differential permeability instead of apparent permeability. This can be proven inductively by calculating the partial derivative of the residual corresponding to the mesh loop in Fig. 6, with respect to the loop flux. All the other entries of the Jacobian can be derived similarly since all the loops have the same structure.

$$\frac{\partial r_x}{\partial \Phi_x} = \sum_{i=1}^4 (\mathcal{R}_i + \frac{\partial \mathcal{R}_i}{\partial \Phi_x} (\Phi_i - \Phi_x)) \quad (8)$$

where, \mathcal{R}_i is the i^{th} reluctance, with the permeability of μ_i and flux density of B_i in the mesh loop. Using the chain rule for each reluctance

$$\frac{\partial \mathcal{R}_i}{\partial \Phi_x} = \frac{\partial \mathcal{R}_i}{\partial \mu_i} \times \frac{\partial \mu_i}{\partial B_i} \times \frac{\partial B_i}{\partial \Phi_x} \quad (9)$$

Considering the formula for a lumped reluctance yields

$$\frac{\partial \mathcal{R}_i}{\partial \mu_i} = -\frac{l}{\mu_i^2 A_i} = -\frac{\mathcal{R}_i}{\mu_i} \quad (10)$$

Using the relationship between flux and flux density yields

$$\frac{\partial B_i}{\partial \Phi_x} = \frac{1}{A_i} \quad (11)$$

Substituting (10) and (11) into (9) and the result into (8) yields

$$\frac{\partial r_x}{\partial \Phi_x} = \sum_{i=1}^4 \mathcal{R}_i (1 - \frac{B_i}{\mu_i} \frac{\partial \mu_i}{\partial B_i}) \quad (12)$$

Differentiating $B_i = \mu_i H_i$ with respect to H_i yields the following equation in which $\mu_{d,i}$ is the differential permeability of the i^{th} reluctance.

$$\frac{\partial B_i}{\partial H_i} = \mu_{d,i} = \mu_i + H_i \frac{\partial \mu_i}{\partial H_i} \quad (13)$$

Using the chain rule

$$\frac{\partial \mu_i}{\partial H_i} = \frac{\partial \mu_i}{\partial B_i} \frac{\partial B_i}{\partial H_i} = \frac{\partial \mu_i}{\partial B_i} \mu_{d,i} \quad (14)$$

Substituting back into (13) yields

$$\mu_{d,i} (1 - \frac{B_i}{\mu_i} \frac{\partial \mu_i}{\partial B_i}) = \mu_i \quad (15)$$

Replacing in 12

$$\frac{\partial r_x}{\partial \Phi_x} = \sum_{i=1}^4 \frac{\mathcal{R}_i \mu_i}{\mu_{d,i}} = \sum_{i=1}^4 \mathcal{R}_{Diff,i} \quad (16)$$

where $\mathcal{R}_{Diff,i}$ represents each reluctance calculated using the differential permeability. (16) corresponds to the diagonal entries of the Jacobian matrix. Nonetheless, the off-diagonal

TABLE 1. Magnetic gear base designs specifications

Parameter	Description	Base Design 1	Base Design 2	Base Design 3	Units
P_1	Rotor 1 pole pairs	11	4	6	
P_3	Rotor 3 pole pairs	45	34	98	
r_o	Active outer radius	150	175	200	mm
T_{BI1}	Rotor 1 back iron thickness	20	35	40	mm
T_{PM1}	Rotor 1 PM thickness	9	5	13	mm
T_{AG1}	Inner air gap thickness	.5	2	1	mm
T_{Mod}	Rotor 2 thickness	11	17	14	mm
T_{Brg}	Bridge thickness	.5	1	1.5	mm
T_{AG2}	Outer air gap thickness	.5	2	1	mm
T_{PM3}	Rotor 3 PM thickness	7	5	7	mm
T_{BI3}	Rotor 3 back iron thickness	20	30	25	mm

entries can be calculated similarly to the approach taken in (8) to (16), which also yields reluctances calculated using the differential permeability. Therefore, (7) can be rewritten as

$$\Phi_{k+1} = \Phi_k - \frac{\mathcal{R}_{App}(\Phi_k) \times \Phi_k - f}{\mathcal{R}_{Diff}(\Phi_k)} \quad (17)$$

Here, $\mathcal{R}_{App}(\Phi_k)$ and $\mathcal{R}_{Diff}(\Phi_k)$ signify the reluctance matrix calculated using the apparent and differential permeabilities, respectively. As a close initial guess for the mesh fluxes improves the robustness and convergence speed for the solver [36], (4) is solved linearly using constant permeabilities to provide the initial guess to begin the Newton-Raphson method. After each iteration, the calculated mesh fluxes are used to compute flux density within each flux tube, which is then utilized to calculate the torque using Maxwell's stress tensor [28]. The flux densities are also used to update the apparent and differential permeabilities of each ferromagnetic node cell based on the B-H curve. The new permeabilities are used to recalculate \mathcal{R}_{App} and \mathcal{R}_{Diff} for the next iteration of (17). Moreover, the matrix factorization method, proposed in [37] is utilized instead of direct inversion in (17) to enhance computational efficiency, numerical stability, and memory usage.

III. EVALUATION

The performance of the MEC model is evaluated by studying the convergence criteria and comparing the torque and flux density predictions with the results from nonlinear FEA models developed in ANSYS Maxwell. First, three diverse magnetic gear base designs, presented in Table 1 and Fig. 7, were used for initial analyses. Additionally, an extensive parametric design optimization study investigated the MEC's capability to analyze and optimize a broad spectrum of design variations in comparison with FEA. These designs, along with the base designs, have the same geometries as those presented in [29] except that they have bridges. (As shown in Fig. 2, these bridges saturate heavily and require nonlinear analysis for accurate torque predictions.) The designs use M250 electrical steel for the ferromagnetic components and NdFeB N42 for the PMs.

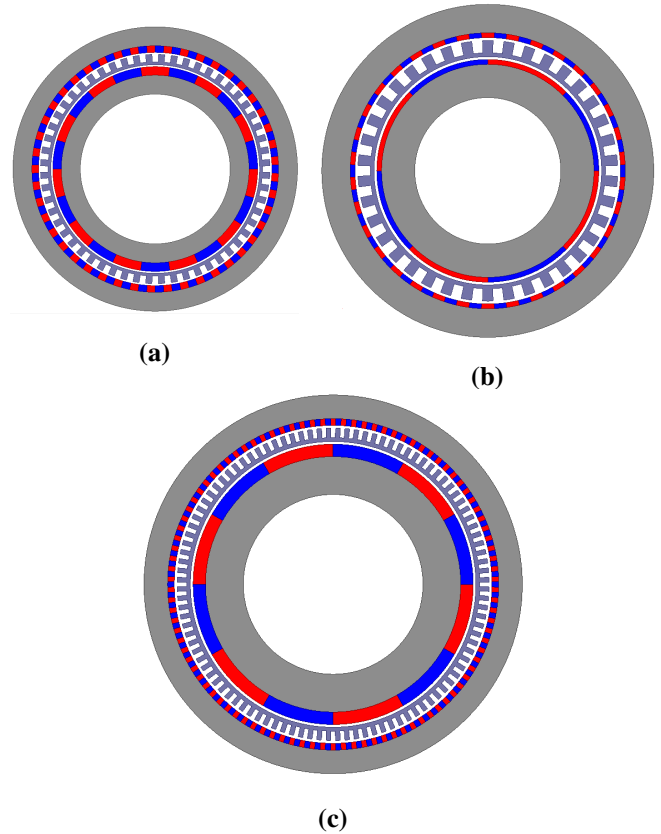


FIGURE 7. Cross-sectional views of base designs (a) 1, (b) 2, and (c) 3. (Airgaps and bridges are enlarged for clarity.)

A. CONVERGENCE CRITERIA

For this study, two parameters are considered as convergence criteria. The first is torque, a critical performance metric in the optimization of MGs. For the solution to be deemed converged, the change in predicted torque between consecutive iterations must be less than 0.1%. This threshold can be adjusted to trade off precision and speed. Fig. III-A depicts the predicted torque after each iteration for three base designs, each normalized by the torque after 10 iterations. For all three base designs, the predicted torque quickly converges. In addition to torque, the root mean square (RMS) of the residual is applied as a secondary convergence criterion. The analysis is considered converged when the RMS of the residual decreases and the torque changes by less than 0.1% between the final two iterations. The RMS of the residual, shown in Fig. III-A, provides an alternative measure of overall solution error, as the elements of $r(\Phi)$ should approach zero during convergence. Using both convergence criteria is essential for a more robust convergence assessment, as the predicted torque might stabilize with less than a 0.1% change while the residual could increase, making the prediction less accurate. Fig. III-A illustrates the total simulation time after each iteration for each of the base designs. The red circles indicate the iteration in which the torque convergence criteria were achieved. Each base design used the fine mesh discretization parameters from [29] to determine the number of radial and

angular layers.

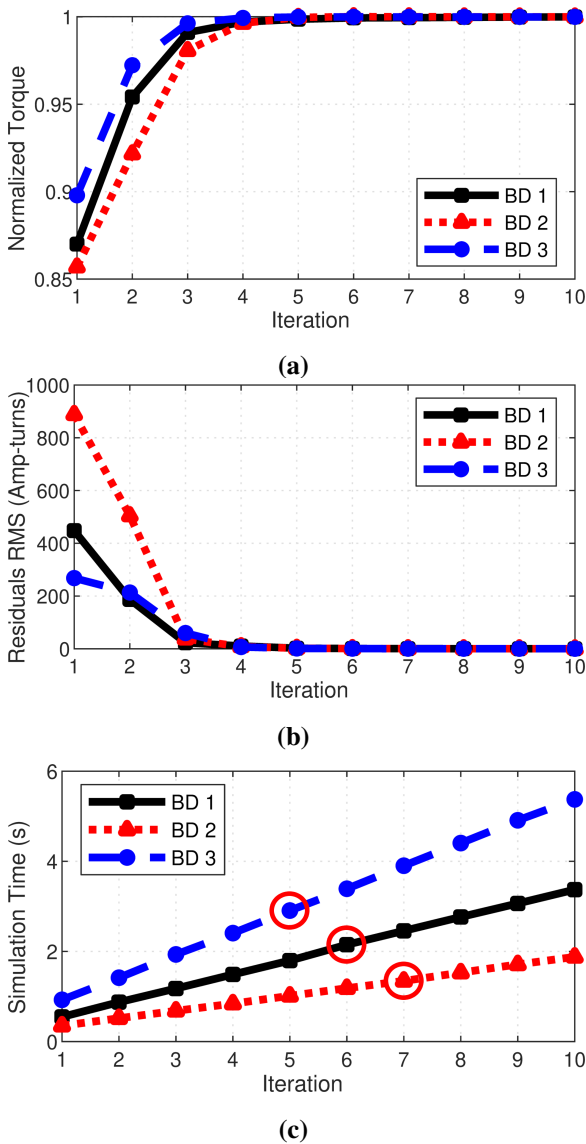


FIGURE 8. For each of the base designs, comparison of (a) normalized torque, (b) RMS of the residual, and (c) total simulation time for different numbers of iterations.

B. OPTIMIZATION STUDY

As demonstrated in [29], insufficient radial and angular layer counts can result in fast models with inaccurate slip torque predictions. Similarly, it is important to assess whether the convergence criteria are effective over a wide range of designs. Therefore, a parametric optimization study of RFMGs with bridges was conducted to evaluate the nonlinear MEC as a rapid design tool. To do so, several critical gear parameters were swept over the ranges of values specified in Table 2, and each of the resulting 140,000 designs was analyzed using the 2D nonlinear MEC model as well as a 2D nonlinear FEA model developed in ANSYS Maxwell, a commercial FEA software. The MEC analysis was done using two different meshing resolutions, specified as the “coarse mesh” and “fine

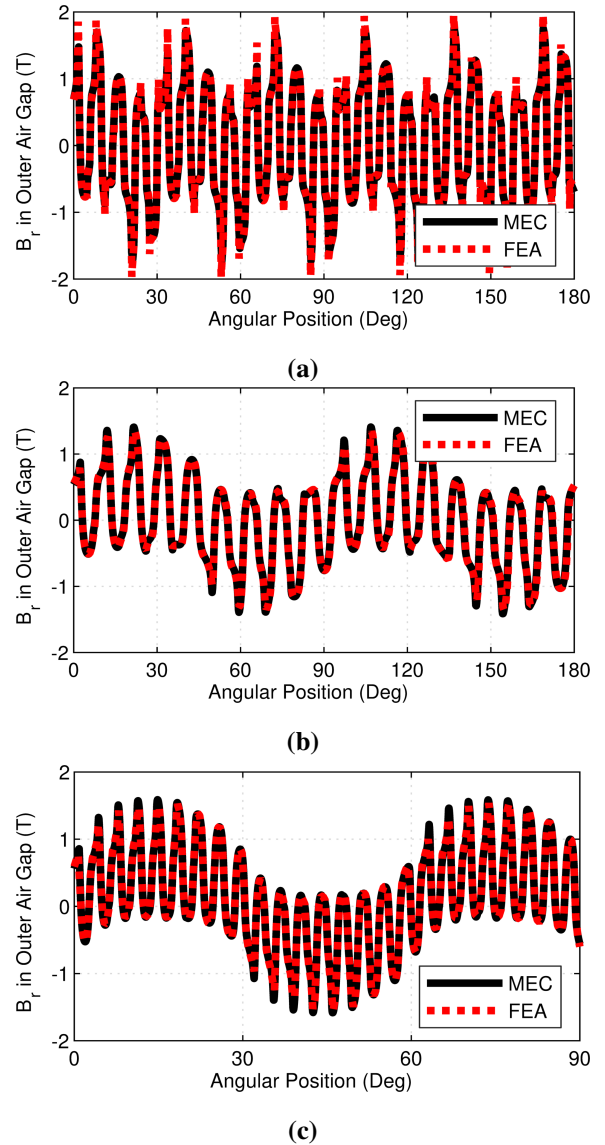


FIGURE 9. Radial flux density along a circular path in the middle of the outer air gap of base designs (a) 1, (b) 2, and (c) 3.

mesh” settings defined in Table 3, with the multipliers defined in [29]. Additionally, both coarse and fine mesh settings use two radial layers in the air regions inside the inner back iron and outside the outer back iron, where flux densities are expected to be relatively small. The bridge, being relatively thin, is also divided into only two radial layers.

As in [29], to reflect the significant interactions between the various dimensions, some were coupled through derived coefficients included in Table 2. The coefficient k_{PM} relates the radial thickness of the Rotor 3 PMs, T_{PM3} , to that of the Rotor 1 PMs, T_{PM1} , as expressed by

$$T_{PM3} = k_{PM} \times T_{PM1} \quad (18)$$

This approach is used because Rotor 3 has a higher PM pole count than Rotor 1, which results in increased flux leakage. Thus, the Rotor 3 PMs should not be thicker than the Rotor

TABLE 2. Parameter sweep ranges for optimization study

Parameter	Description	Ranges of Values	Units
G_r	Integer part of gear ratio	5,9,17	
P_1	Inner pole pairs		
	For $G_r = 5$	4,5,6,...18	
	For $G_r = 9$	3,4,5,...13	
	For $G_r = 17$	3,4,5,...8	
r_O	Active outer radius	150, 175, 200	mm
k_{BI1}	Rotor 1 back iron thickness coefficient	0.4, 0.5, 0.6	
T_{PM1}	Rotor 1 PM thickness	3.5, 7, ...13	mm
T_{AG}	Air gap thickness (per gap)	1.5	mm
T_{Mods}	Rotor 2 thickness	11, 14, 17	mm
T_{BrG}	Bridge thickness	0.5, 1, 1.5	mm
k_{PM}	Rotor 3 PM thickness ratio	0.5, 0.75, 1	
T_{BI3}	Rotor 3 back iron thickness	20, 25, 30	mm

TABLE 3. Magnetic Gear MEC Model Discretization Settings for the Optimization Study

Settings	Coarse Mesh	Fine Mesh
Angular layers multiplier	10	30
Radial layers in the rotor 1 back iron	3	3
Rotor 1 magnets radial layers multiplier	10	20
Inner air gap radial layers multiplier	10	20
Modulators radial layers multiplier	10	20
Outer air gap radial layers multiplier	10	20
Rotor 3 magnets radial layers multiplier	10	20
Radial layers in the rotor 3 back iron	3	3
Minimum radial layers in rotor 1 magnets	3	3
Minimum radial layers in inner air gap	3	3
Minimum radial layers in rotor 2	3	5
Minimum radial layers in outer air gap	3	3
Minimum radial layers in rotor 3 magnets	3	5

1 PMs. Additionally, the coefficient, k_{BI1} , couples the radial thickness of the Rotor 1 back iron to the Rotor 1 pole arc to prevent excessive saturation, according to

$$T_{BI1} = k_{BI1} \left(\frac{\pi r_{BI1}}{P_1} \right) \quad (19)$$

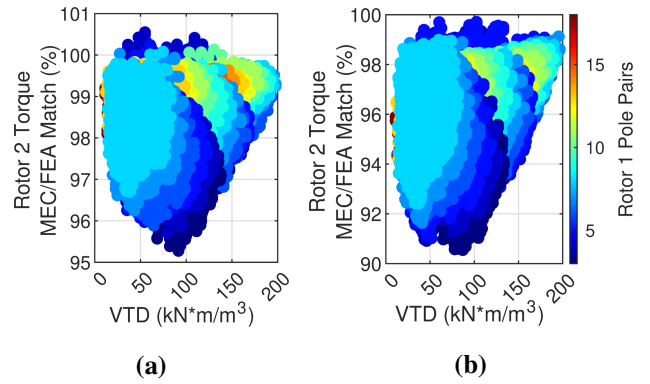
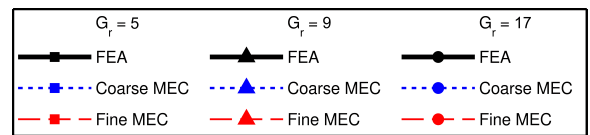
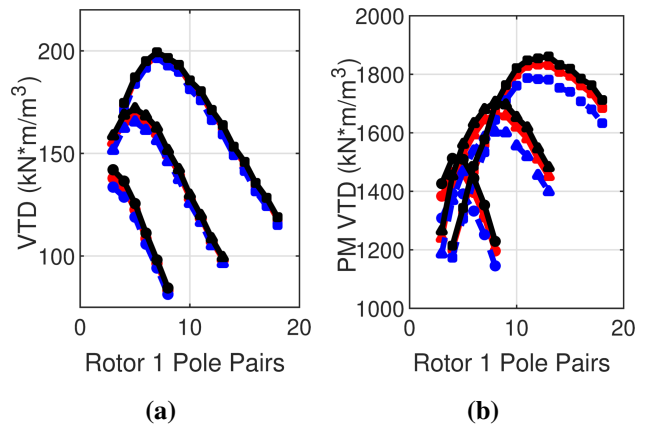
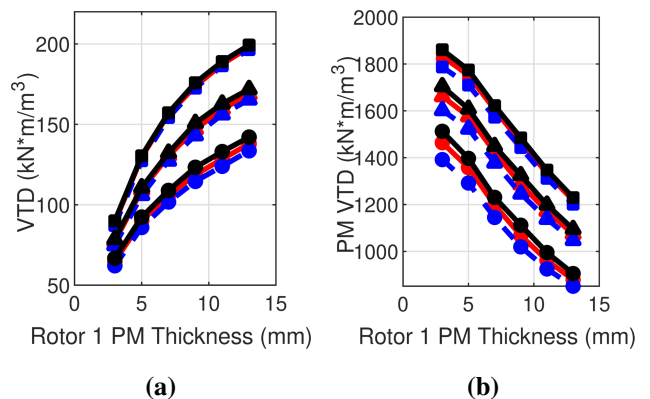
where r_{BI1} is the outer radius of the Rotor 1 back iron, as in [29]. Furthermore, G_r represents the integer part of the gear ratio and relates the pole pair counts according to

$$P_3 = \begin{cases} (G_{int} - 1)P_1 + 1, & G_{int}P_1 \text{ odd} \\ (G_{int} - 1)P_1 + 2, & G_{int}P_1 \text{ even} \end{cases} \quad (20)$$

This avoids integer gear ratios and designs lacking symmetry, which are prone to large torque ripples [2] and unbalanced magnetic forces on the rotors [33], respectively.

The graphs in Figs. 10-13 and the statistics in Table 4 compare the optimization study results obtained from the fine and coarse-meshed MEC with those from the FEA.

Fig. 10 demonstrates the accuracy of the MEC models across the entire 140,000-design parametric sweep, indicating their fair accuracy over a wide range of volumetric torque densities (VTDs). Overall, the torque predictions from both fine and coarse mesh MEC models closely correspond to those from FEA models, with discrepancies less than 5%


FIGURE 10. MEC agreement with FEA over the full parametric sweep range with the (a) fine mesh and the (b) coarse mesh.

FIGURE 11. Legend for design trend plots in Figs. 12 and 13

FIGURE 12. Impact of Rotor 1 pole pair count on the maximum achievable (a) VTD and (b) PM VTD.

FIGURE 13. Impact of Rotor 1 PM thickness on the maximum achievable (a) VTD and (b) PM VTD.

and 10%, respectively. Notably, the MEC models exhibit closer agreement with the FEA for designs with higher VTDs,

TABLE 4. Summary of optimization study results

Metric	Fine Mesh MEC	Coarse Mesh MEC	FEA
Minimum Discrepancy	-4.7%	-9.45%	N/A
Maximum Discrepancy	0.55%	-0.29%	N/A
Average Discrepancy	1.54%	4.33%	N/A
Average Absolute Discrepancy	1.54%	4.33%	N/A
Total Simulation Time (sec)	387,500	60,822	6,003,857
Average Simulation Time (sec)	2.77	0.43	42.89

indicating that the accuracy is best for the designs most likely to be of interest. Specifically, for the designs with the top 10% of VTDs, the maximum absolute discrepancies are 2% and 4.5% for fine and coarse mesh MEC models, respectively. Figs. 12 and 13 indicate the MEC model’s accurate tracking of key performance trends, particularly in VTD and PM VTD (defined as slip torque divided by PM material volume) relative to the Rotor 1 pole pair count and PM thickness. Table 4 presents a statistical analysis demonstrating the accuracy and speed of the coarse and fine mesh MEC models compared to the FEA model across the entire parametric design space outlined in Table 2. On average, the fine and coarse mesh MEC models are about 15 and 100 times as fast as the FEA, respectively.

IV. CONCLUSION

This study presents a fast and robust 2D nonlinear MEC model for radial flux magnetic gears. First, the systematic implementation and analysis of the MEC model are presented. Then, the model is shown to quickly and accurately predict torque and air gap flux densities for a wide range of RFMG designs with highly saturated bridges. The modeling begins with discretizing the RFMG into mesh loops. The system of equations is built by applying mesh-flux analysis on each mesh loop and constructing the reluctance matrix of the RFMG. The resulting system of equations is nonlinear since the reluctance matrix is a function of mesh fluxes. To solve the nonlinear system, Newton-Raphson, an iterative method, is shown to be a fast and reliable approach. The combination of requiring the RMS of the residual to decrease between the last two iterations and requiring the torque variation between the last two iterations to be less than 0.1% proves to be an effective convergence criterion. For three diverse base designs with bridges, the nonlinear MEC agrees very well with FEA on the air gap flux densities. A parametric optimization study with 140,000 designs shows that the nonlinear MEC consistently agrees with FEA on torque predictions and accurately tracks design trends. The results demonstrate that the presented model is able to achieve 15 to 100 times faster analysis while maintaining an average discrepancy of 1.54% and 4.53% relative to the FEA model’s torque predictions for the fine and coarse meshed MECs, respectively.

REFERENCES

[1] G. Tao *et al.*, “Experimental comparison of acoustic characteristics for a high-efficiency magnetic gearbox and a mechanical planetary gearbox for

industrial hvac applications,” *IEEE Trans. Energy Convers.*, vol. 39, no. 1, pp. 182–190, 2024.

[2] N. W. Frank and H. A. Toliyat, “Gearing ratios of a magnetic gear for wind turbines,” in *Proc. IEEE Int. Electr. Mach. Drives Conf.*, 2009, pp. 1224–1230.

[3] K. Li *et al.*, “Designing and experimentally testing a magnetic gearbox for a wind turbine demonstrator,” *IEEE Trans. Ind. Appl.*, vol. 55, pp. 3522–3533, July 2019.

[4] A. B. Kjaer, S. Korsgaard, S. S. Nielsen, L. Demsa, and P. O. Rasmussen, “Design, fabrication, test, and benchmark of a magnetically geared permanent magnet generator for wind power generation,” *IEEE Trans. Energy Convers.*, vol. 35, pp. 24–32, Mar. 2020.

[5] K. K. Uppalapati, J. Z. Bird, D. Jia, J. Garner, and A. Zhou, “Performance of a magnetic gear using ferrite magnets for low speed ocean power generation,” in *Proc. IEEE Energy Convers. Congr. Expo.*, 2012, pp. 3348–3355.

[6] P. O. Rasmussen, T. V. Frandsen, K. K. Jensen, and K. Jessen, “Experimental evaluation of a motor-integrated permanent-magnet gear,” *IEEE Trans. Ind. Appl.*, vol. 49, no. 2, pp. 850–859, 2013.

[7] T. V. Frandsen, P. O. Rasmussen, and K. K. Jensen, “Improved motor integrated permanent magnet gear for traction applications,” in *Proc. IEEE Energy Convers. Congr. Expo.*, 2012, pp. 3332–3339.

[8] T. V. Frandsen *et al.*, “Motor integrated permanent magnet gear in a battery electrical vehicle,” *IEEE Trans. Ind. Appl.*, vol. 51, no. 2, pp. 1516–1525, 2015.

[9] P. Chmelicek, S. D. Calverley, R. S. Dragan, and K. Atallah, “Dual rotor magnetically geared power split device for hybrid electric vehicles,” *IEEE Trans. Ind. Appl.*, vol. 55, no. 2, pp. 1484–1494, 2019.

[10] P. O. Rasmussen, H. H. Mortensen, T. N. Matzen, T. M. Jahns, and H. A. Toliyat, “Motor integrated permanent magnet gear with a wide torque-speed range,” in *Proc. IEEE Energy Convers. Congr. Expo.*, 2009, pp. 1510–1518.

[11] T. F. Talerico, Z. A. Cameron, J. J. Scheidler, and H. Hasseeb, “Outer stator magnetically-geared motors for electrified urban air mobility vehicles,” in *Proc. AIAA/IEEE Electr. Aircr. Technol. Symp.*, 2020, pp. 1–25.

[12] R. S. Dragan, R. E. Clark, E. K. Hussain, K. Atallah, and M. Odavic, “Magnetically geared pseudo direct drive for safety critical applications,” *IEEE Trans. Ind. Appl.*, vol. 55, no. 2, pp. 1239–1249, 2019.

[13] G. Puchhammer, “Magnetic gearing versus conventional gearing in actuators for aerospace applications,” in *Proc. Aero. Mech. Symp.*, 2014, pp. 175–181.

[14] V. M. Asnani, J. J. Scheidler, and T. F. Talerico, “Magnetic gearing research at nasa,” in *Proc. AHS Int. Annu. Forum*, 2018, pp. 1–14.

[15] J. J. Scheidler, V. M. Asnani, and T. F. Talerico, “Nasa’s magnetic gearing research for electrified aircraft propulsion,” in *Proc. AIAA/IEEE Electr. Aircr. Technol. Symp.*, 2018, pp. 1–12.

[16] J. J. Scheidler, Z. A. Cameron, and T. F. Talerico, “Dynamic testing of a high-specific-torque concentric magnetic gear,” in *Proc. Vertical Flight Soc. Annu. Forum*, 2019, pp. 1–8.

[17] T. F. Talerico, Z. A. Cameron, J. J. Scheidler, and H. Hasseeb, “Outer stator magnetically-geared motors for electrified urban air mobility vehicles,” in *Proc. AIAA/IEEE Electr. Aircr. Technol. Symp.*, 2020, pp. 1–25.

[18] B. Praslicka, M. C. Gardner, M. Johnson, and H. A. Toliyat, “Review and analysis of coaxial magnetic gear pole pair count selection effects,” *IEEE J. Emerg. Sel. Top. Power Electron.*, vol. 10, no. 2, pp. 1813–1822, 2022.

[19] B. Praslicka *et al.*, “Design and analysis of an axial flux coaxial magnetic gear with balanced axial forces for precision aerospace actuation application,” in *Proc. IEEE Energy Convers. Congr. Expo.*, 2022, pp. 1–8.

[20] H. Y. Wong, H. Baninajar, B. W. Dechant, P. Southwick, and J. Z. Bird, “Experimentally testing a halbach rotor coaxial magnetic gear with 279 nm/l torque density,” *IEEE Trans. Energy Convers.*, vol. 38, no. 1, pp. 507–518, 2023.

[21] M. Johnson *et al.*, “Design, construction, and analysis of a large-scale inner stator radial flux magnetically geared generator for wave energy conversion,” *IEEE Trans. Ind. Appl.*, vol. 54, no. 4, pp. 3305–3314, 2018.

[22] H. Baninajar *et al.*, “Designing a halbach rotor magnetic gear for a marine hydrokinetic generator,” *IEEE Trans. Ind. Appl.*, vol. 58, no. 5, pp. 6069–6080, 2022.

[23] S. A. Khan, G. Duan, and M. C. Gardner, “Comparison of modulator retention shapes for radial flux coaxial magnetic gears,” in *Proc. IEEE Energy Convers. Congr. Expo.*, 2022, pp. 1–7.

[24] E. Gouda, S. Mezani, L. Baghli, and A. Rezzoug, “Comparative study between mechanical and magnetic planetary gears,” *IEEE Trans. Magn.*, vol. 47, no. 2, pp. 439–450, 2011.

- [25] X. Ran, J. Shang, M. Zhao, and Z. Yi, "Improved configuration proposal for axial reluctance resolver using 3-d magnetic equivalent circuit model and winding function approach," *IEEE Trans. Transp. Electrification*, vol. 9, no. 1, pp. 311–321, 2023.
- [26] G. Vidanalage, B. D. Silva, A. Lombardi, J. Tjong, and N. C. Kar, "Magnetic field-based induction machine modeling incorporating space and time harmonic effects," *IEEE Access*, vol. 12, pp. 41 579–41 589, 2024.
- [27] P. Wu and Y. Sun, "A hybrid model for calculating on-load performance of delta-type ipm machines accounting for rotor and stator saturation," *IEEE Trans. Ind. Electron.*, pp. 1–11, 2024.
- [28] M. Johnson, M. C. Gardner, and H. A. Toliyat, "A parameterized linear magnetic equivalent circuit for analysis and design of radial flux magnetic gears—part i: Implementation," *IEEE Trans. Energy Convers.*, vol. 33, pp. 784–791, June 2018.
- [29] —, "A parameterized linear magnetic equivalent circuit for analysis and design of radial flux magnetic gears—part ii: Evaluation," *IEEE Trans. Energy Convers.*, vol. 33, pp. 792–800, June 2018.
- [30] H. Diab, Y. Amara, and G. Barakat, "A 3d nonlinear magnetic equivalent circuit model for an axial field flux focusing magnetic gear: Comparison of fixed-point and newton–raphson methods," *Mathematics and Computers in Simulation*, vol. 224, pp. 119–137, 2024.
- [31] M. Fukuoka, K. Nakamura, and O. Ichinokura, "Dynamic analysis of planetary-type magnetic gear based on reluctance network analysis," *IEEE Trans. Magn.*, vol. 47, no. 10, pp. 2414–2417, 2011.
- [32] R. Benlamine, T. Hamiti, F. Vangraefschepe, F. Dubas, and D. Lhotellier, "Modeling of a coaxial magnetic gear equipped with surface mounted pms using nonlinear adaptive magnetic equivalent circuits," in *Proc. IEEE Int. Conf. Elect. Mach.*, 2016, pp. 1888–1894.
- [33] G. Jungmayr, J. Loeffler, B. Winter, F. Jeske, and W. Amrhein, "Magnetic gear: Radial force, cogging torque, skewing and optimization," in *Proc. IEEE Energy Convers. Congr. Expo.*, 2015, pp. 898–905.
- [34] S. Gerber and R.-J. Wang, "Analysis of the end-effects in magnetic gears and magnetically geared machines," in *Proc. Int. Conf. Electr. Mach.*, 2014, pp. 396–402.
- [35] S.-H. Lee, S.-Y. Im, J.-Y. Ryu, and M.-S. Lim, "Optimum design process of coaxial magnetic gear using 3d performance prediction method considering axial flux leakage," *IEEE Trans. Ind. Appl.*, vol. 60, no. 2, pp. 3075–3085, 2024.
- [36] S. C. Chapra and R. P. Canale, *Numerical Methods for Engineers.*, 7th ed. McGraw Hill, 2015.
- [37] T. A. Davis, "Algorithm 930: Factorize: An object-oriented linear system solver for matlab," *ACM Trans. Math. Softw.*, vol. 39, no. 4, pp. 1–18, Jul. 2013.

DANIAL KAZEMIKIA earned his B.Sc. degree in electrical engineering from K. N. Toosi University, Tehran, Iran in 2019. He is currently a Ph.D. student in electrical engineering at the University of Texas at Dallas. His research interests are computational electromagnetics, design optimization, and physics-informed neural networks focusing on the design and control of electric machines and magnetic gears.

MATTHEW C. GARDNER earned his B.S. in electrical engineering from Baylor University, Waco, Texas in 2014. He earned his Ph.D. in electrical engineering from Texas A&M University, College Station, Texas in 2019. In August 2020, he joined the University of Texas at Dallas, where he is an assistant professor. His research interests include optimal design and control of electric machines and magnetic gears.

...